AIMS Materials Science, 12(1): 85–100.
DOI: 10.3934/matersci.2025007
Received: 30 November 2024
Revised: 19 January 2025
Accepted: 06 February 2025
Published: 10 February 2025

http://www.aimspress.com/journal/Materials

Research article

Microstructure and thermophysical properties of NiTiZr phase change alloys for downhole tool heat storage

Wentao Qu[1,*], Qian Zhang[1], Guibian Li[2], Boyang Pan[3] and Haiying Liu[1]

[1] School of Mechanical Engineering, Xi'an Shiyou University, Xi'an 710065, China
[2] Shanxi Fenglei Drilling Tools Co., Ltd.Houma 043013, China
[3] School of Materials Science and Engineering, Beihang University, Beijing 100191, China

* **Correspondence:** Email: wtqu@xsyu.edu.cn.

Abstract: To overcome the limitations of solid-liquid phase change materials, such as liquid leakage, unstable shape, and serious corrosion at elevated temperatures, the design of a solid-solid phase change material using Ni-Ti-Zr as a metal element was utilized for its high thermal conductivity and stability to provide new thermal storage solutions for downhole tools. The influence of Zr content on the thermophysical properties and microstructure of the material was also investigated. The results showed that the designed solid-solid phase change material could reach 4129.93 × 10^6 $J^2K^{-1}s^{-1}m^{-4}$ quality factor, which was much higher than most of the phase change materials. This was attributed to the increase in Zr content, where Zr atoms took the place of Ti atoms, creating vacancy defect and leading to the distortion of the alloy lattice where the Ti_2Ni phase gradually became the $(Ti, Zr)_2Ni$ phase, the rise in density and enthalpy of the phase transition, and the increase in the temperature of the phase transition. When the Zr content was 12%, the phase transition temperature of the alloy matched the downhole working temperature, demonstrating excellent thermal cycling stability, and is expected to be a heat storage material for downhole tools.

Keywords: NiTiZr; solid-solid phase change material; microstructure; thermal energy storage

1. Introduction

With the development and exploitation of oil and gas fields gradually moving deeper, and the depletion of shallow oil and gas fields in the ground, oil companies are gradually shifting their focus

to the exploration and exploitation of ultra-deep wells. However, ultra-deep well surveys are constrained by various factors such as high temperature and pressure [1,2], complex formations, ultra-long wellbores, corrosion [3,4], and higher demands on downhole tool performance. The logging instrument is an indispensable tool for the oil and gas resources industry to obtain downhole information by measuring downhole temperature, pressure, porosity, and other parameters to determine the location of the oil field and reserves; however, it often faces problems such as heat leakage from the external high-temperature environment and defects in the internal self-heating of the electronic devices, resulting in the temperature of the electronics in the logging instrument to exceed the design temperature rapidly and failing to work [5].

Downhole tools usually use solid-liquid phase change materials (SL-PCM) for temporary thermal storage [6,7], which effectively extends the uptime of downhole electronics [8], but SL-PCM has the disadvantages of low thermal storage density, phase separation, and low heat absorption rate [9], which largely limits the temperature control effect of the thermal management system of logging instrument; this greatly limits the temperature control effect of the thermal management system of the logging instrument; Song et al. used graphite to reduce the supercooling of $MgCl_2·6H_2O$ from 40.6 to 29.4 °C, while the thermal conductivity was significantly improved [10]; Li et al. successfully solved the supercooling and phase separation problems of $CaCl_2·6H_2O$-$MgCl_2·6H_2O$ eutectic salt by adjusting the ratios of the nucleating agent and the thickening agent [11]; and Wu et al. prepared $Na_2SO_4·10H_2O$-$Na_2HPO_4·12H_2O$ stoichiometric composite phase change materials using porous SiO_2 and expanded graphite [12,13], which effectively solved the phenomena of overcooling and phase segregation of phase change materials. However, SL-PCM has serious defects such as liquid leakage and easy reacts with containers when in the liquid state; thus, SL-PCM must be encapsulated when in use, which inevitably leads to a reduction in the volumetric storage capacity of the system and an increase in the production cost [14].

The solid-solid phase change materials (SS-PCM) have the advantages of high heat storage density, simple heat storage structure, high reliability, no power drive, and are not affected by other factors, which are particularly suitable for temperature control in high-temperature fields such as aerospace and petroleum industries [15,16]. Fukahori et al. found that compared with the conventional molten-salt phase change materials [17], Al-Si alloys have a higher heat storage capacity and a higher thermal conductivity, which is more suitable for high-temperature superconducting heat storage materials; Shharar D et al. found that NiTi can be used as a high power material substitute for 1-octadecanoic without sacrificing the bulk heat capacity [18]; and Kato1 et al. investigated the latent heat values of Ni-Ti alloys with different compositions and found that the latent heat values of Ni-Ti alloys are greater than those of other SMAs and can reach 35 J/g [19]. However, the isotonic ratio of the Ni-Ti alloys has phase transition temperatures below 100 °C and cannot be applied in high-temperature environments [20,21]. Li et al. developed ultra-high performance high-temperature Ni-Mn-Ti PCMs using a martensitic phase transition strategy [22]. The latent heat of Ni-Mn-Ti SS-PCMs was in the range of 43–65 J/g. Hite et al. utilized a shape memory alloy Ni-Ti-Hf as a solid-solid phase transition material since $Ni_{50.3}Ti_{29.7}Hf_{20}$ exhibits a high enthalpy of transformation of 32.5 J/g and a thermal conductivity of 11.19 $Wm^{-1}K^{-1}$ [23]. Nevertheless, the phase transition temperatures of these ternary alloys are too high to be suitable as heat storage materials for downhole high-temperature environments. It is well known that adding an appropriate amount of Zr element to the Ni-Ti alloy can significantly improve the mechanical properties and martensitic phase transition temperature. The Ni-Ti-Zr ternary alloy not only has a lower cost but also has the advantages of high

thermal conductivity and no risk of leakage as a phase change material, which makes it an ideal thermal energy storage material. Moreover, solid-solid phase change materials are relatively lacking in downhole applications; thus, it is of great significance to utilize the Ni-Ti-Zr ternary alloy as a solid-solid phase change material for the thermal control of downhole tools.

We focus on the high-temperature environment of the downhole, Zr as a substitute of Ti element, designing an $Ni_{49.5}Ti_{50.5-x}Zr_x$ (x = 8, 10, 12, 15 at.%) alloy, and exploring new thermal storage materials for downhole tools. We also investigate the effect of different Zr content on the thermophysical properties and microstructure of the material. Finally, we use the thermophysical properties of alloys after multiple alternations of hot and cold environments to verify the thermal cycling stability of materials.

2. Materials and methods

2.1. Material preparation

$Ni_{49.5}Ti_{50.5-x}Zr_x$ (x = 8, 10, 12, 15 at.%) alloy button ingots were fabricated by arc melting under argon protection using high purity Ni (99.99%), Ti (99.98%) and Zr (99.99%) elements as raw materials. To ensure homogeneity of the material composition, the ingots were repeatedly melted at least six times. The button ingots were then sealed into quartz tubes filled with argon gas and homogenized at 1223 K for 2 h, followed by water cooling. Samples of different sizes were cut from the ingots by electro-discharge machining for various experimental measurements.

2.2. Microstructure characterization

X-ray diffraction patterns (XRD) were obtained utilizing a Rigaku diffractometer (D8 Advance), equipped with Cu-Kα radiation, to analyze the phase compositions of the investigated alloys. The chemical composition from selected sample areas was analyzed with an EDS detector. Scanning electron microscopy (SEM, Zeiss Gemini 360) was used to analyze the surface features. The SEM samples were incrementally ground using SiC papers (400–3000 grit) to obtain a scratch-free surface before ultrasonic cleaning with acetone and ethanol for 10 min and drying with cold air, which was then chemically etched with Kroll's reagent (5 mL of HF, 25 mL of HNO_3, and 50 mL of H_2O).

2.3. Thermophysical property analysis

2.3.1. Density measurements and ethics approval of research

The densities of samples with different compositions were measured using the Archimedes' method. The samples of size 10 × 10 × 1.5 mm^3 were first weighed in air (denoted as w_a) and then immersed in water and weighed again (denoted as w_s). The density (ρ) of the measured samples was determined by $\rho = \rho_w w_a/(w_a - w_s)$, where ρ_w is the density of water.

2.3.2. Measurement of phase transition temperatures and thermophysical parameters

The phase transition temperature and the enthalpy change of the phase transition were determined by differential scanning calorimetry measurements (DSC25) at a heating/cooling rate of 20 °Cmin^{-1} over a temperature range of –40 to 450 °C. The specific heat capacity was measured by the modulated DSC technique, utilizing sapphire with a well-known specific heat capacity as a standard sample. The thermal cycling stability of $Ni_{49.5}Ti_{38.5}Zr_{12}$ PCM was examined by DSC measurements during 100 cycles of heating and cooling between –40 and 130 °C at 10 °C min^{-1}.

2.3.3. Thermal conductivity and mechanical behavior measurement

Thermal diffusivity was measured using the laser flash method (NETZSCH, LFA467). Square samples with dimensions of 10 × 10 × 1.5 mm^3 were used. Measurements were carried out at several temperatures during the heating for the phase change to occur. The thermal conductivity k was obtained by $k = Cp \cdot \rho \cdot \alpha$, where Cp, ρ, and α are the specific heat capacity, density, and thermal diffusivity. The specimen was measured by an HV-50A hardness tester with a load of 100 N and a retention time of 15 s.

3. Results and discussion

3.1. Microscopic morphology analysis

Figure 1a–d shows the scanning electron microscopy images of Ti-Ni-Zr alloys with different Zr contents. The smooth (Ti, Zr)Ni matrix and austenite phase can be seen in all the images, in addition to some Ti_2Ni-type phases. With the increase of Zr content, the Ti_2Ni-type phases gradually decrease, and the Ti_2Ni-type phase around the second phase gradually turns into a gray color [24]. The gray zone should originate from the amplitude-modulated decomposition of the single-phase solid solution at high temperatures during cooling and the corresponding consists of the elements Ti, Ni, and Zr. From the EDS results in Table 1, the gray zone may be $(Ti, Zr)_2Ni$. On the other hand, with the increase of Zr content, the austenite phase is gradually connected into flakes from a single vesicle, and the $(Ti, Zr)_2Ni$ phase is mostly distributed in the grain boundaries or within the grains. This is mainly due to the displacement of small-sized Ti atoms by large-sized Zr atoms, creating vacancy defects and causing redistribution of Zr and Ti atoms in the B2 phase, which in turn leads to distortion of the lattice, and the small vesicular matrix phase is squeezed and connected into sheets.

Figure 2 shows the XRD patterns of $Ni_{49.5}Ti_{50.5-x}Zr_x$ alloys (x = 8, 10, 12, 15 at.%) at room temperature. It can be seen that all the alloys have a $(Ti, Zr)_2Ni$ phase and austenite B2 and martensite B19’ phases, with the observed diffraction peaks of the Ni-Ti binary alloys exhibiting a high degree of similarity to the aforementioned position. The crystal surface indices corresponding to the main diffraction peak of XRD are (210), (220), (020), and (132) crystal planes, respectively. When the Zr content is 8% and 10%, the Ni atoms preferentially bind with the Ti atoms to form the Ti_2Ni phase. With the addition of the Zr element, the Ni-Ti lattice is distorted [25], and when the Zr content exceeds 12%, the residual Ni atoms diffuse into the TiNi matrix to form a Ni-rich region, which combines with Zr atoms to form the NiZr phase [26]. This promotes the formation of the B2 phase and the Ti_2Ni phase, and the Ti_2Ni phase gradually becomes the $(Ti, Zr)_2Ni$ phase, and the diffraction peak is shifted to the

left. Furthermore, the $(Ti, Zr)_2Ni$ and Ti_2Ni phases are body-centered cubic (BCC) lattice structures, and the NiZr phase is a face-centered cubic (FCC) lattice structure.

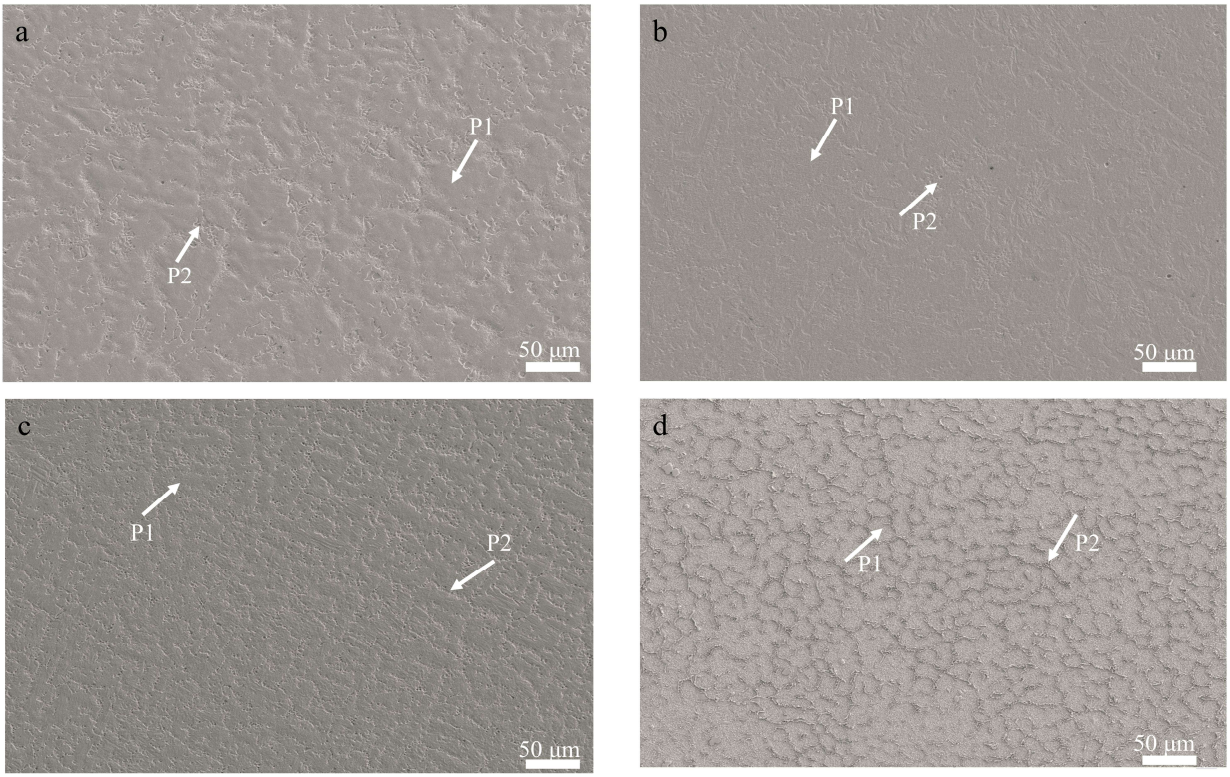

Figure 1. The SEM diagram for different materials. (a) $Ni_{49.5}Ti_{42.5}Zr_8$; (b) $Ni_{49.5}Ti_{40.5}Zr_{10}$; (c) $Ni_{49.5}Ti_{38.5}Zr_{12}$; and (d) $Ni_{49.5}Ti_{35.5}Zr_{15}$.

Table 1. Chemical composition results of Ni-Ti-Zr alloys with different Zr contents.

Zr content (at.%)	P1 zone (matrix phase) (at.%)				P2 zone (gray zone) (at.%)			
	Ni	Ti	Zr	Ti + Zr/Ni	Ni	Ti	Zr	Ti + Zr/Ni
8	49.81	42.52	7.67	1.0076	30.52	65.72	3.76	2.2765
10	49.62	40.66	9.72	1.0153	34.67	56.61	8.72	1.8843
12	49.71	38.23	12.06	1.0117	33.59	52.34	14.07	1.9771
15	49.69	35.53	14.78	1.0125	30.88	49.79	19.33	2.2383

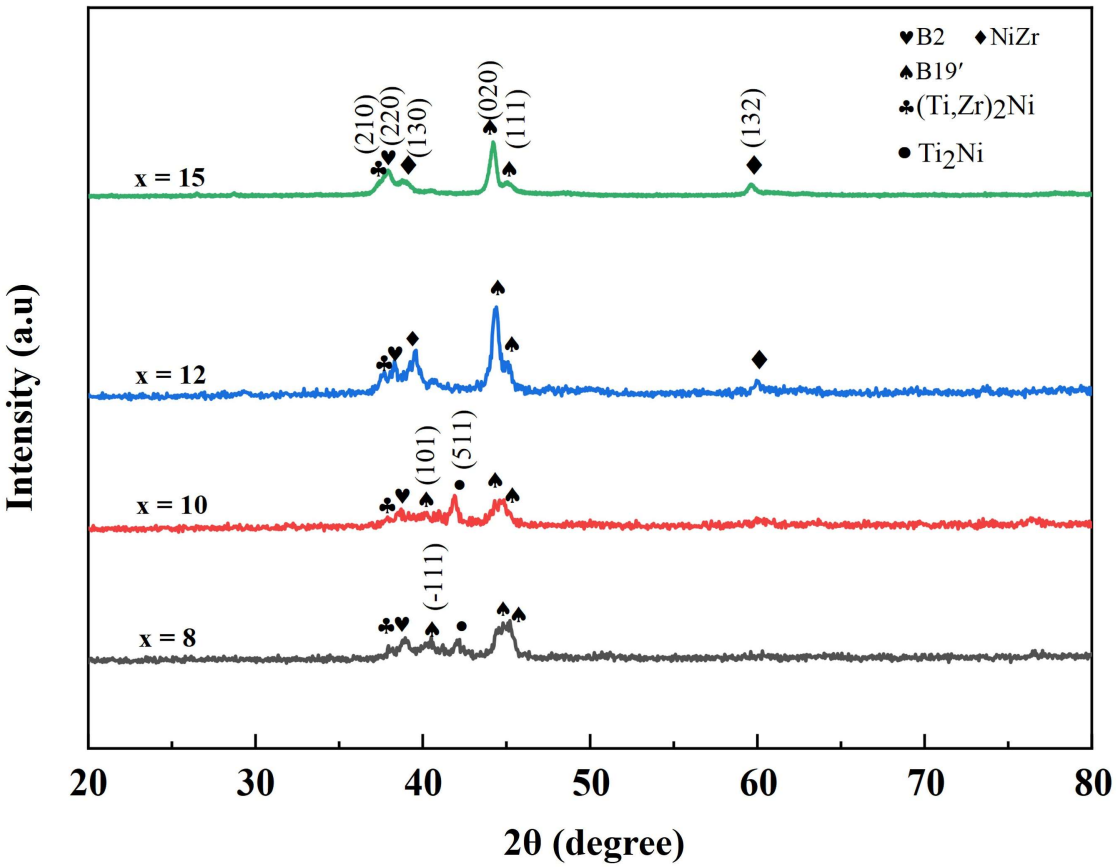

Figure 2. XRD patterns of $Ni_{49.5}Ti_{50.5-x}Zr_x$ (x = 8, 10, 12, 15 at.%)

3.2. Temperature and enthalpy of phase change

The differential scanning calorimetry (DSC) curves of $Ni_{49.5}Ti_{50.5-x}Zr_x$ (x = 8, 10, 12, 15 at.%) are shown in Figure 3a. It can be seen that all materials have heat absorption peaks during the temperature rise and exothermic peaks during the temperature reduction, corresponding to the reversible phase transformation processes of the low-temperature martensitic phase and the high-temperature austenitic phase [22]. With the increase of the Zr content, the heat absorption peaks of these solid-solid phase transition alloys shift to the right, which implies an increase in the onset temperature of the phase transformation. When the Zr content is in the range of 8%–10%, the phase transformation onset temperatures are increased slightly, and when the Zr content is 10%–15%, the phase transition onset temperature increases significantly. Based on the results of DSC, the onset and end temperatures of the forward and reverse phase transitions of these PCMs (M_s, M_f, A_s, and A_f) are determined using the tangent method; the results are shown in Figure 3b. The A_s for x = 8 is 11 °C and that for x = 15 is 144 °C. This shows that the phase transition temperature is increased by about 20 °C for each 1% increase in Zr content, indicating that the replacement of Ti by Zr can increase the phase transition temperature of the alloy [27,28].

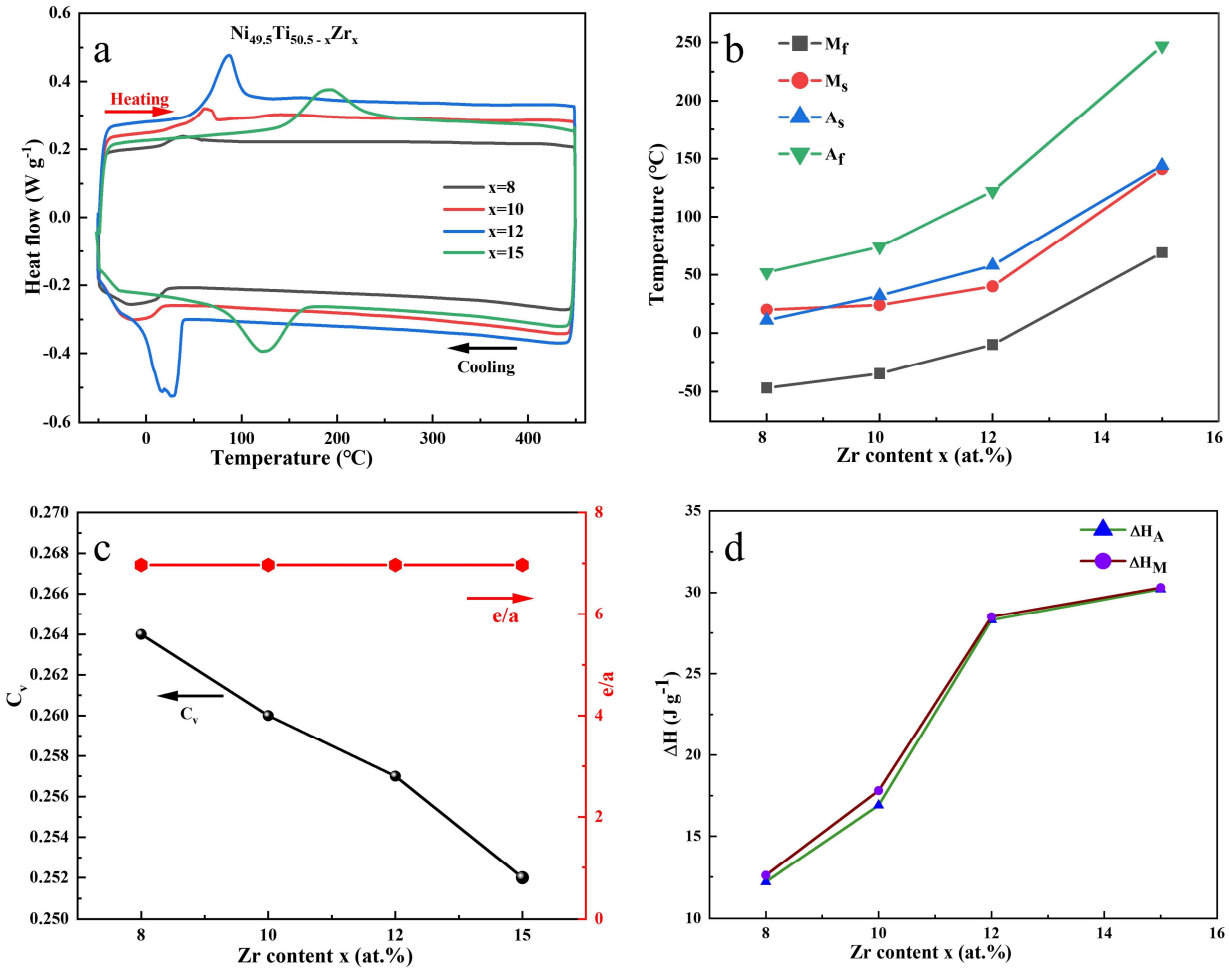

Figure 3. Thermal parametric results of $Ni_{49.5}Ti_{50.5-x}Zr_x$ (x = 8, 10, 12, 15 at.%) SS-PCMs. (a) DSC curves. (b) Forward (M_s and M_f) and reverse (A_s and A_f) phase transition temperatures versus Ti content x curves. (c) Curves of average valence electron number e/a and average valence electron concentration Cv with Ti content x. (d) Curves of phase transition enthalpy with Ti content x.

Figure 3c shows the variation curves of average valence electron number e/a and average valence electron concentration C_v with Zr content. The average valence electron number (e_v/a) and the average valence electron concentration (C_v) can be expressed using Eqs 1 and 2, respectively: f_{Ni}, f_{Ti}, and f_{Zr} represent the atomic fraction of the Ni, Ti, and Zr atoms in the Ni-Ti-Zr alloy; e_v^{Ni}, e_v^{Ti} and e_v^{Zr} represent the valence electron number of Zr atoms of Ti atoms of Ni, respectively; Z^{Ni}, Z^{Ti} and Z^{Zr} represent the atomic number of the Ni, Ti, and Zr atoms, respectively. With the increase of Zr content, the average valence electron number e/a of each alloy does not change, but the average valence electron concentration C_v of the alloys gradually decreases. This is mainly due to Ti and Zr belonging to the same family, with the same number of outermost electrons and different atomic numbers, which lead to an increase in the phase transition temperature.

$$\frac{e_v}{a} = f_{Ni}e_v^{Ni} + f_{Ti}e_v^{Ti} + f_{Zr}e_v^{Zr} \quad (1)$$

$$C_v = \frac{e_v}{e_t} = \frac{f_{Ni}e_v^{Ni} + f_{Ti}e_v^{Ti} + f_{Zr}e_v^{Zr}}{f_{Ni}Z^{Ni} + f_{Ti}Z^{Ti} + f_{Zr}Z^{Zr}} \quad (2)$$

The enthalpy changes (which equals the latent heat L) associated with the forward and reverse phase transitions, denoted as ΔH_M and ΔH_A, respectively, are obtained by integrating the areas of the exothermic and absorptive peaks on the DSC curves (Figure 3a), and the results are shown in Figure 3d. It is seen that the enthalpy change value increases gently with the increase of Zr content x when the Zr content is 8% to 10%. When the Zr content exceeds 12%, the enthalpy change value grows more rapidly, up to about 30 J g^{-1}, which shows a more favorable performance.

3.3. Density

Figure 4 shows the density as a function of Zr content x. It can be seen that the density of the alloys increases linearly with increasing Zr content x. The density of all compositions ranges from 6.55–6.78g·cm^{-3} due to the replacement of the low-density Ti (4.54 g·cm^{-3}) by the high-density Zr (6.49g·cm^{-3}). The densities of these metallic SS-PCMs have much higher densities than the organic, inorganic, and hydrated salt PCMs (typically 0.10–2.50 g·cm^{-3}). In addition, the red dashed line shows a linear regression model of the trend of the density fitted with the Zr content, which is given by the following equation: $\rho = 0.03356 \times Zr + 6.26159$, where ρ is density in g/cm^3 and Zr is hafnium content in at.%. Due to the small variation of the Zr content, there is some error between the measured density values and the calculated prediction from the fitted curve.

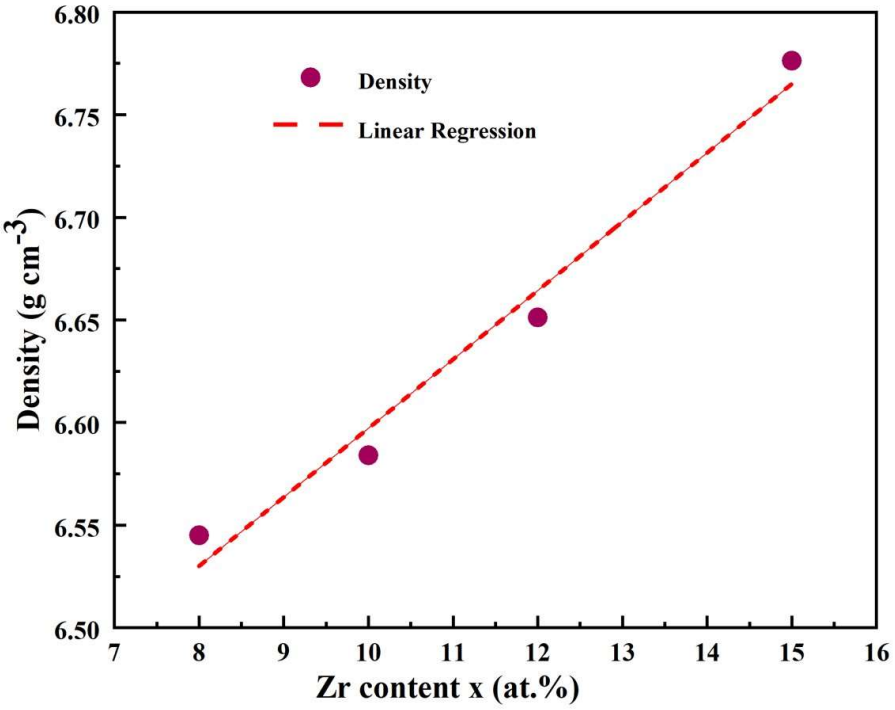

Figure 4. Density as a function of Zr content x for the $Ni_{49.5}Ti_{50.5-x}Zr_x$ (x = 8, 10, 12, 15 at.%) SS-PCMs.

3.4. Specific heat capacity and thermal conductivity

Figure 5a–d shows the curves of specific heat capacity C_p and thermal conductivity k versus temperature T for different materials. From the left axis, it can be seen that for different material compositions, the C_p versus temperature T curves exhibit similar shapes. When the phase transformation occurs, the C_p rises with the temperature up to the peak temperature, and when it exceeds the peak temperature, the C_p starts to show a downward trend, which is the same as that exhibited by the DSC images of each material. The C_p value rapid increase is due to the increase in the enthalpy of the phase transition during the reverse martensitic phase transformation, so the specific heat capacity C_p in the range of the phase transformation does not represent the true C_p value [29]. After the completion of the phase transformation, the C_p value of each material is almost the same at high versus low temperatures, which is 0.49–0.52 $Jg^{-1}K^{-1}$. This overall trend is consistent with the specific heat capacity trend in NiTi SMA [30], which suggests that the C_p values may be independent of the composition of the high and low temperature phases.

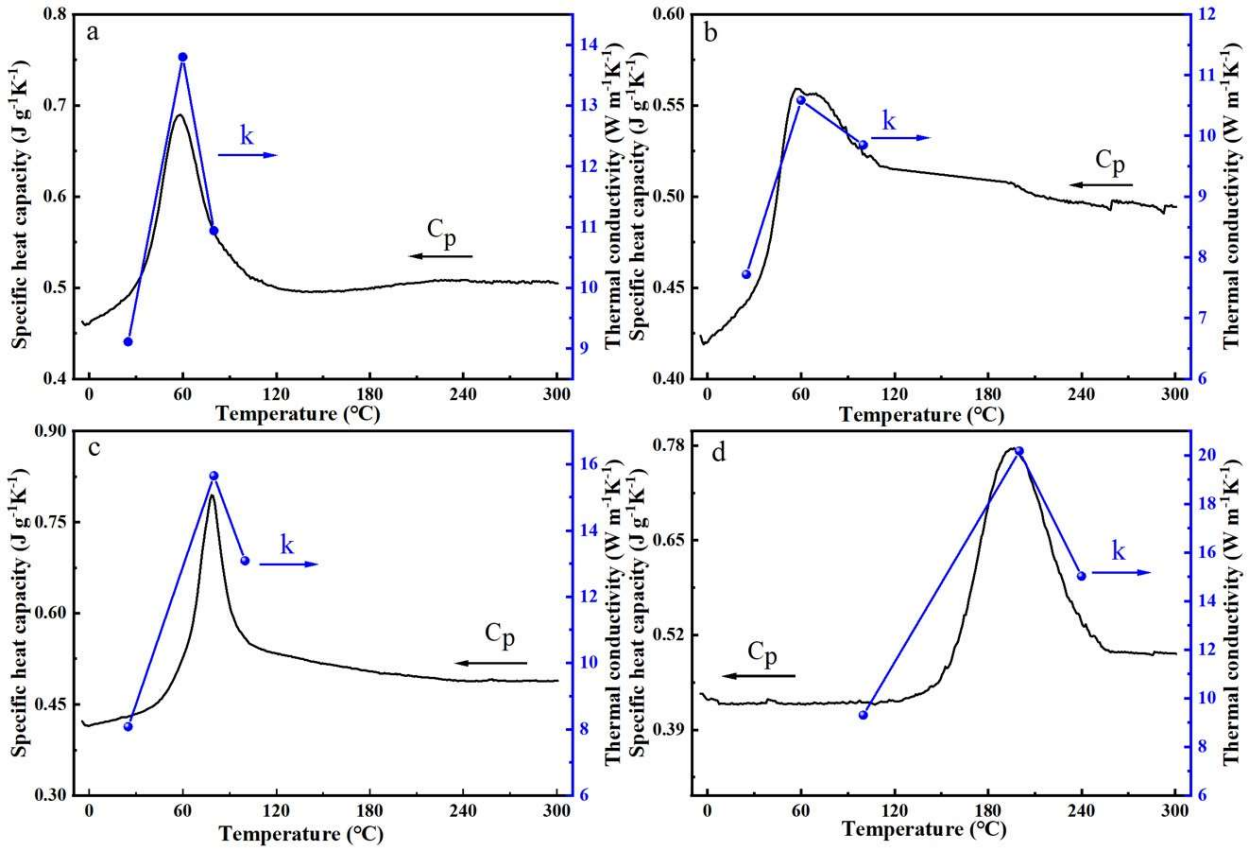

Figure 5. Variation curves of specific heat capacity C_p and thermal conductivity k with temperature for different materials. (a) $Ni_{49.5}Ti_{42.5}Zr_8$. (b) $Ni_{49.5}Ti_{40.5}Zr_{10}$. (c) $Ni_{49.5}Ti_{38.5}Zr_{12}$. (d) $Ni_{49.5}Ti_{35.5}Zr_{15}$.

As seen from the right axis of Figure 5a–d, the thermal conductivity k exhibits the same trend as the specific heat capacity C_p at different temperatures. Before the phase transition occurs, the thermal conductivity k is about 8–10 W $m^{-1}K^{-1}$ at low temperatures, whereas during heating to undergo the

phase transition, k exhibits a linear increase with increasing temperature. This could be due to the increase in electronic thermal conductivity due to the change in carrier mobility during the phase transition [31]. After the completion of the phase transition, it decreases slightly as the temperature increases, and the value of k at high temperatures is about 12 W $m^{-1}K^{-1}$, which is much higher than that of the thermal conductivity of the conventional organic materials (commonly 0.1–2.0 W $m^{-1}K^{-1}$). From Table 2, it can be seen that the thermal conductivity of the Ni-Ti-Zr alloy is higher compared to traditional organic paraffin. The reason for this is that the molecular interactions in paraffin are relatively weak, and the molecular chains are long, leading to a lower efficiency in heat transfer. The high thermal conductivity of the Ni-Ti-Zr alloy can be attributed to the following reasons: The Ti_2Ni phase in the alloy has a BCC lattice structure, which is relatively dense. Moreover, heat transfer primarily relies on lattice vibrations. The $(Ti, Zr)_2Ni$ phase has a FCC lattice structure, which has a higher thermal conductivity. This lattice structure is less sparse than the Ti_2Ni phase, which facilitates better heat transfer. According to the XRD pattern, the increase in Zr content promotes the formation of the $(Ti, Zr)_2Ni$ phase, thereby enhancing heat transfer. As a result, the thermal conductivity K of the alloy increases progressively. As the temperature increases, the lattice vibrations in the $(Ti, Zr)_2Ni$ phase are more strongly excited by heat, increasing the lattice vibrations and further improving the thermal conductivity of the alloy.

Table 2. Thermophysical parameters of heat storage materials

Title	Density/g·cm^{-3}	Specific heat capacity /J g^{-1} K^{-1}	Thermal conductivity /W $m^{-1}K^{-1}$	Latent heat /J g^{-1}
organic paraffin	0.82	2.011	0.15	210
$Ni_{49.5}Ti_{42.5}Zr_8$	6.55	0.492	13.80	12.6
$Ni_{49.5}Ti_{40.5}Zr_{10}$	6.58	0.443	10.59	17.8
$Ni_{49.5}Ti_{38.5}Zr_{12}$	6.65	0.431	15.65	28.3
$Ni_{49.5}Ti_{35.5}Zr_{15}$	6.78	0.423	20.17	30.2

We compare this with the commonly used thermal storage material (organic paraffin) to investigate the feasibility of Ni-Ti-Zr alloy as a heat storage material for downhole tools. The thermophysical parameters of paraffin and the alloy are shown in Table 2. It can be seen that the latent heat value of the paraffin is higher than that of the Ni-Ti-Zr alloy, but the Ni-Ti-Zr alloy has a high density, and more heat is stored under the same mass, which is favorable for use in a limited space and is expected to be used for downhole heat storage tools. Moreover, the high thermal conductivity of the Ni-Ti-Zr alloy indicates that the heat is transferred faster inside the alloy. The quality factor (FOM) as a quantifiable measure of PCM performance is usually given by the Eq 3：

$$FOM = k \times \rho \times L \tag{3}$$

where k, ρ, and L are the thermal conductivity, density, and latent heat of phase transition, respectively [32,33]. Calculating the FOM values of Ni-Ti-Zr alloys with different compositions according to Eq 3 gives a quality factor of up to 4129.93×10^6 $J^2K^{-1}s^{-1}m^{-4}$, which is much higher than existing organic paraffins. This provides a theoretical basis for thermal energy storage in metal-solid-solid phase-change materials.

3.5. Thermal cycle analysis and mechanical properties

The thermal cycling stability of the thermophysical properties of PCMs is critical for their practical thermal storage applications when working in downhole high-temperature environments [34]. The thermal cycling stability of $Ni_{49.5}Ti_{38.5}Zr_{12}$ SS-PCM is investigated by measuring the DSC curves during 100 heating and cooling processes of the material. Figure 6a shows the results of $Ni_{49.5}Ti_{38.5}Zr_{12}$ SS-PCM after 100 rapid heating and cooling cycles at 10 °Cmin^{-1}. It can be seen that the peak of DSC gradually shifts to the left with the increase in the number of thermal cycles and stabilizes after several thermal cycles in which the reverse phase transition temperatures (A_s and A_f) slightly decrease during the thermal cycles; the forward phase transition temperatures (M_s and M_f) remain almost unchanged during the cycles. Its thermophysical parameters after multiple thermal cycles are shown in Figure 6b, where the enthalpy change values ΔH_M (for forward phase change) and ΔH_A (for reverse phase change) remain unchanged during multiple thermal cycles. Ni-Ti-Zr alloy heat is released during the transition to martensite, but when cooled by the reverse transition from martensite down to autensite, the heat is absorbed. In this process, the heat is caused by the internal phase transition of the alloy, which involves atomic rearrangement, structural change, lattice dislocation, and other processes that are symmetrical, resulting in roughly the same heat absorbed or released by each phase transition without the loss or increase of heat. Thus, the latent heat of the forward/reverse martensitic phase transition, in this study, is almost equivalent. This indicates the superior thermal cycling stability of Ni-Ti-Zr SS-PCM, making it a strong candidate for heat storage materials for downhole tools.

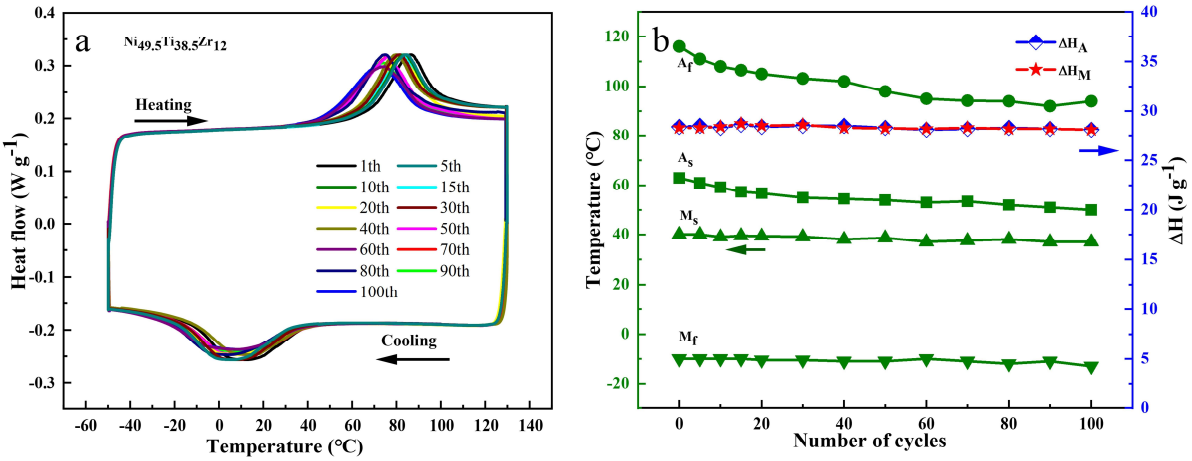

Figure 6. Thermal cycling stability of phase transition and thermophysical properties. (a) DSC curves of $Ni_{49.5}Ti_{38.5}Zr_{12}$ SS-PCM during multiple thermal cycles across phase transition. (b) Variation of corresponding phase transition temperatures (M_s, M_f, A_s, and A_f) and enthalpy changes of phase transitions (ΔH_M and ΔH_A) of $Ni_{49.5}Ti_{38.5}Zr_{12}$ SS-PCM with the number of cycles.

From Figure 7, the hardness of Ni-Ti-Zr alloy gradually increases in the process of 1 to 20 thermal cycles, which promotes the precipitation of the enhanced phase or the refinement of the grains. When the number of thermal cycles reaches 30 times, the precipitate may dissolve or redistribute, and the alloy shows a higher hardness. However, when the number of thermal cycles exceeds 30 times, the hardness of the alloy does not increase because the grain has reached a certain uniformity, and the precipitation reinforcement tends to balance. When the number of thermal cycles continues to increase,

the hardness of the Ni-Ti-Zr alloy begins to decrease, possibly because the excessive thermal cycles lead to excessive dissolution of the precipitate or the formation of an unstable phase, which reduces the hardness of the alloy [35,36].

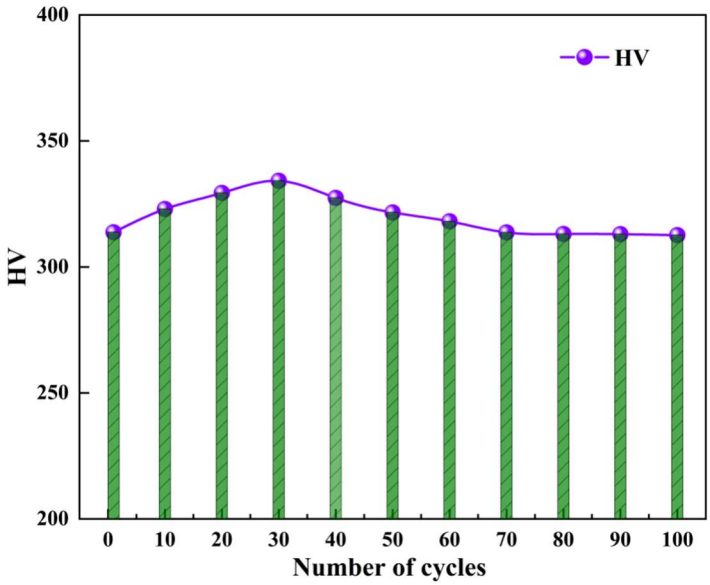

Figure 7. Curve of the $Ni_{49.5}Ti_{38.5}Zr_{12}$ SS-PCM hardness with the number of cycles.

4. Conclusions

The thermophysical parameters of $Ni_{49.5}Ti_{50.5-x}Zr_x$ (x = 8, 10, 12, 15 at%) SS-PCMs were investigated due to the advantages of metallic phase change materials such as high thermal conductivity and density. The effect of different contents of Zr on their thermophysical parameters was analyzed, and our major conclusions are as follows:

1. The microscopic morphology reveals the presence of a (Ti, Zr)Ni matrix and a small amount of Ti_2Ni phase, and with the increase of Zr, the Ti_2Ni phase gradually becomes the $(Ti, Zr)_2Ni$ phase. Moreover, the Zr content is in the range of 8%~15%, the enthalpy of the phase transition of the alloy with the increase in the Zr content of x increases, and when the Zr content is more than 12%, the enthalpy of phase transition can reach around $30Jg^{-1}$. This is attributed to the fact that the addition of the Zr element induces distortion in the Ni-Ti lattice and hinders the martensitic transformation, thus promoting the increase of the enthalpy of phase transition.

2. $Ni_{49.5}Ti_{50.5-x}Zr_x$ SS-PCMs quality factor FOM have a maximum value of $4129.93 \times 10^6 J^2K^{-1}s^{-1}m^{-4}$, and the phase transition temperature of these SS-PCMs can be adjusted by controlling the elemental composition ratio. When the Zr content is 12%, the temperature range required for the phase transformation meets the requirements of downhole working conditions. After 100 rapid heating and cooling cycles, the phase transformation temperature of the material decreases slightly, but the enthalpy change value is almost unchanged, which indicates that the material has good thermal cycling stability.

3. Metal phase change materials for heat storage have no risk of leakage and exhibit better heat storage performance than conventional SL-PCMs, and Ni-Ti-Zr alloys offer a potential option as SS-PCMs for heat storage in downhole tools. The phase change material studied in this paper can be

applied to the special thermos, mainly to absorb the heat generated by the electronic devices when the logging instrument works.

4. Thermal cycle times can increase the hardness of the alloy within a certain range. Thus, the Ni-Ti-Zr alloy has 30 thermal cycles with the highest hardness and the strongest deformation resistance. Therefore, this material is applied to the log instrument to withstand a large load and high underground pressure.

Use of AI tools declaration

The authors declare they have not used Artificial Intelligence (AI) tools in the creation of this article.

Funding

This work was supported by the National Natural Science Foundation of China (No. 52071261).

Acknowledgments

The authors are grateful for the financial support from the National Natural Science Foundation of China (No. 52071261).

Author contributions

Conceptualization: W.Q.; methodology: Q.Z.; validation: H.L. and G.L.; formal analysis: Q.Z.; investigation: Q.Z. and B.P.; resources: H.L.; data curation: Q.Z.; writing—original draft preparation: Q.Z. and H.L; writing—review and editing: Q.Z. and B.P.; visualization: H.L.; supervision: W.Q. and G.L. All authors have read and agreed to the published version of the manuscript.

Conflict of interest

The authors declare no conflict of interest.

References

1. Zhang Y, Xu M, Song J, et al. (2022) Study on the corrosion change law and prediction model of cement stone in oil wells with CO_2 corrosion in ultra-high-temperature acid gas wells. *Constr Build Mater* 323: 125879. https://doi.org/10.1016/j.conbuildmat.2021.125879
2. Li H, Zhang X, Qi D, et al. (2015) Failure analysis of the adhesive metal joint bonded on anticorrosion plastic alloy composite pipe. *Eng Fail Anal* 47: 49–55. https://doi.org/10.1016/j.engfailanal.2014.09.009
3. Peng Z, Lv F, Feng Q, et al. (2022) Enhancing the CO_2-H_2S corrosion resistance of oil well cement with a modified epoxy resin. *Constr Build Mater* 326: 126854. https://doi.org/10.1016/j.conbuildmat.2022.126854

4. Qu W, Pan B, Gong H, et al. (2023) Electrochemical corrosion and impedance studies of Ti-30Zr-xNb (x = 7, 10, 13 at.%) alloy in simulated downhole environment. *J Solid State Electr* 27: 1155–1164. https://doi.org/10.1007/s10008-023-05430-z
5. Xue Z, Zhang C, Li Z, et al. (2022) An on-site temperature prediction method for passive thermal management of high-temperature logging apparatus. *Meas Control* 55: 1180–1189. https://doi.org/10.1177/00202940221076809
6. Liu Y, Zheng R, Li J (2022) High latent heat phase change materials (PCMs) with low melting temperature for thermal management and storage of electronic devices and power batteries: Critical review. *RSER* 168: 112783. https://doi.org/10.1016/j.rser.2022.112783
7. Sharma RK, Ganesan P, Tyagi V (2016) Long-term thermal and chemical reliability study of different organic phase change materials for thermal energy storage applications. *J Therm Anal Calorim* 124: 1357–1366. https://doi.org/10.1007/s10973-016-5281-5
8. Peng J, Deng C, Wei F, et al. (2023) A hybrid thermal management system combining liquid cooling and phase change material for downhole electronics. *J Energy Storage* 72: 108610. https://doi.org/10.1016/j.est.2023.108610
9. Yang X, Li C, Ma Y, et al. (2023) High thermal conductivity of porous graphite/paraffin composite phase change material with 3D porous graphite foam. *Chem Eng J* 473: 145364. https://doi.org/10.1016/j.cej.2023.145364
10. Song Z, Deng Y, Li J, et al. (2018) Expanded graphite for thermal conductivity and reliability enhancement and supercooling decrease of $MgCl_2·6H_2O$ phase change material. *Materials Res Bull* 102: 203–208. https://doi.org/10.1016/j.materresbull.2018.02.024
11. Li G, Zhang B, Li X, et al. (2014) The preparation, characterization and modification of a new phase change material: $CaCl_2·6H_2O$-$MgCl_2·6H_2O$ eutectic hydrate salt. *Sol Energ Mat Sol C* 126: 51–55. https://doi.org/10.1016/j.solmat.2014.03.031
12. Wu Y, Wang T (2015) Hydrated salts/expanded graphite composite with high thermal conductivity as a shape-stabilized phase change material for thermal energy storage. *Energy Convers Manage* 101: 164–171. https://doi.org/10.1016/j.enconman.2015.05.006
13. Wu Y, Wang T (2014) Preparation and characterization of hydrated salts/silica composite as shape-stabilized phase change material via sol-gel process. *Thermochim Acta* 591: 10–15. https://doi.org/10.1016/j.tca.2014.07.012
14. Zhang N, Yuan Y, Cao X, et al. (2018) Latent heat thermal energy storage systems with solid-liquid phase change materials: A review. *Adv Eng Mater* 20: 753. https://doi.org/10.1002/adem.201700753
15. Shamberger PJ, Bruno NM (2020) Review of metallic phase change materials for high heat flux transient thermal management applications. *Appl Energy* 258: 113955. https://doi.org/10.1016/j.apenergy.2019.113955
16. Fernandes D, Pitié F, Cáceres G, et al. (2012) Thermal energy storage: "How previous findings determine current research priorities". *Energy* 39: 246–257. https://doi.org/10.1016/j.energy.2012.01.024
17. Fukahori R, Nomura T, Zhu C, et al. (2016) Thermal analysis of Al-Si alloys as high-temperature phase-change material and their corrosion properties with ceramic materials. *Appl Energy* 163: 1–8. https://doi.org/10.1016/j.apenergy.2015.10.164

18. Sharar DJ, Leff AC, Wilson A, et al. (2021) High-capacity high-power thermal energy storage using solid-solid martensitic transformations. *Appl Therm Eng* 187: 116490. https://doi.org/10.1016/j.applthermaleng.2020.116490
19. Kato H (2021) Latent heat storage capacity of NiTi shape memory alloy. *J Mater Sci* 56: 8243–8250. https://doi.org/10.1007/s10853-021-05777-6
20. Li G, Bao J, Yu T, et al. (2024) An atomistic study of effects of temperature and Ni element on the phase transition and wear behavior of NiTi shape memory alloy. *Tribol Int* 192: 109309. https://doi.org/10.1016/j.triboint.2024.109309
21. Frenzel J, George EP, Dlouhy A, et al. (2010) Influence of Ni on martensitic phase transformations in NiTi shape memory alloys. *Acta Mater* 58: 3444–3458. https://doi.org/10.1016/j.actamat.2010.02.019
22. Li S, He L, Lu H, et al. (2023) Ultrahigh-performance solid-solid phase change material for efficient, high-temperature thermal energy storage. *Acta Mater* 249: 118852. https://doi.org/10.1016/j.actamat.2023.118852
23. Hite N, Sharar DJ, Trehern W, et al. (2021) NiTiHf shape memory alloys as phase change thermal storage materials. *Acta Mater* 218: 117175. https://doi.org/10.1016/j.actamat.2021.117175
24. Li J, Yi X, Sun K, et al. (2018) The effect of Zr on the transformation behaviors, microstructure and the mechanical properties of Ti-Ni-Cu shape memory alloys. *J Alloys Compd* 747: 348–353. https://doi.org/10.1016/j.jallcom.2018.03.053
25. Evirgen A, Karaman I, Santamarta R, et al. (2016) Relationship between crystallographic compatibility and thermal hysteresis in Ni-rich NiTiHf and NiTiZr high temperature shape memory alloys. *Acta Mater* 121: 374–383. https://doi.org/10.1016/j.actamat.2016.08.065
26. Hsieh SF, Hsue AWJ, Chen SL, et al. (2013) EDM surface characteristics and shape recovery ability of $Ti_{35.5}Ni_{48.5}Zr_{16}$ and $Ni_{60}Al_{24.5}Fe_{15.5}$ ternary shape memory alloys. *J Alloys Compd* 571: 63–68. https://doi.org/10.1016/j.jallcom.2013.03.111
27. Kornegay SM, Kapoor M, Hornbuckle BC, et al. (2021) Influence of H-phase precipitation on the microstructure and functional and mechanical properties in a Ni-rich NiTiZr shape memory alloy. *Mater Sci Eng A* 801: 140401. https://doi.org/10.1016/j.msea.2020.140401
28. Karakoc O, Atli KC, Evirgen A, et al. (2020) Effects of training on the thermomechanical behavior of NiTiHf and NiTiZr high temperature shape memory alloys. *Mater Sci Eng A* 794: 139857. https://doi.org/10.1016/j.msea.2020.139857
29. Zhu J, Wu H, Wu Y, et al. (2021) Influence of Ni_4Ti_3 precipitation on martensitic transformations in NiTi shape memory alloy: R phase transformation. *Acta Mater* 207: 116665. https://doi.org/10.1016/j.actamat.2021.116665
30. Cheng F, Hu L, Reddy JN, et al. (2014) Temperature-dependent thermal properties of a shape memory alloy/MAX phase composite: Experiments and modeling. *Acta Mater* 68: 267–278. https://doi.org/10.1016/j.actamat.2013.12.014
31. Zheng Q, Zhu G, Diao Z, et al. (2019) High contrast thermal conductivity change in Ni-Mn-In heusler alloys near room temperature. *Adv Eng Mater* 21: 1342. https://doi.org/10.1002/adem.201801342
32. Trehern W, Hite N, Ortiz-Ayala R, et al. (2023) NiTiCu shape memory alloys with ultra-low phase transformation range as solid-state phase change materials. *Acta Mater* 260: 119310. https://doi.org/10.1016/j.actamat.2023.119310

33. Liu G, Li S, Song C, et al. (2024) High-entropy Ti-Zr-Hf-Ni-Cu alloys as solid-solid phase change materials for high-temperature thermal energy storage. *Intermetallics* 166: 108177. https://doi.org/10.1016/j.intermet.2023.108177
34. Long Z, Tao P, Kong L, et al. (2023) Effect of cryogenic thermal cycling on the microstructure and mechanical properties of Zr-based bulk metallic glasses. *Mater Sci Eng A* 863: 144513. https://doi.org/10.1016/j.msea.2022.144513
35. Wu SK, Chang YC (2019) Thermal cycling effect on transformation temperatures of different transformation sequences in TiNi-based shape memory alloys. *Materials* 12: 12–16. https://doi.org/10.3390/ma12162512
36. Swaminathan G, Sampath V, Santosh S (2024) Effect of cobalt addition on thermal cycling behaviour of $Ti_{50}Ni_{(50-x)}cox$ shape memory alloys. *Phys Scr* 99: 23–28. https://doi.org/10.1088/1402-4896/ad23b5

AIMS Press